Dual-Site Mg^{2+} Substitution in $LaFeO_3$ ceramics: Defect Engineering and Multifunctional Property Modulation

Subhajit Nandy,[1,*] Sayan Ghosh,[2] Vikasmita Samanta,[2] Mya Theingi,[2] Keun Hwa Chae,[3]
and C. Sudakar[2,*]

[1]Deutsches Elektronen-Synchrotron DESY, Notkestr. 85, 22607 Hamburg, Germany
[2]Multi-Functional Materials Laboratory, Department of Physics, Indian Institute of Technology Madras, Chennai 600036, India
[3]Advanced Analysis and Data Center, Korea Institute of Science and Technology, Seoul 02792, Republic of Korea

* Corresponding authors E-mail addresses: subhajit.nandy@desy.de, and csudakar@iitm.ac.in

Abstract: Pristine $LaFeO_3$ and Mg^{2+}-incorporated La-deficient $LaFeO_3$ ($La_{1-x}FeO_{3-\delta}$; xMg, x = 0.2, 0.4) and Fe-deficient $LaFeO_3$ ($LaFe_{1-x}O_{3-\delta}$; xMg, x = 0.2, 0.4) ceramics were synthesized from nanoparticles prepared *via* a low-temperature citrate sol-gel process. X-ray diffraction (XRD) confirms the formation of a single-phase in pristine $LaFeO_3$, while minor secondary phases are observed in Mg^{2+}-incorporated, La- and Fe-deficient compositions. Raman spectroscopy reveals distinct vibrational modes in Mg^{2+}-incorporated La-deficient $LaFeO_3$, whereas Fe-deficient variants exhibit featureless spectra. Diffuse reflection spectral measurements show a bandgap of 2.34 eV for pristine $LaFeO_3$, which narrows to 2.23 and 2.30 eV upon Mg^{2+}-incorporation in La-deficient $LaFeO_3$. Conversely, Fe-deficient, Mg^{2+}-incorporated $LaFeO_3$ exhibit broad absorption without a defined band-edge, suggesting the presence of defect states or mid-gap levels. Magnetic measurements at room temperature indicate a marked enhancement in magnetization (7.6 emu/g) in La-deficient compositions, indicative of emergent ferromagnetism, while Fe-deficient samples show weak ferromagnetism (1.2 emu/g), comparable to pristine $LaFeO_3$ (0.7 emu/g). O K-edge X-ray absorption spectroscopy reveals changes in Fe(3d)–O(2p), La(5d)–O(2p), and Fe(4sp)–O(2p) hybridizations. XANES analysis at the La L_3 and Fe K edges confirms the retention of La^{3+} and Fe^{3+} oxidation states. Local structural studies indicate site-specific Mg^{2+} substitution and the generation of oxygen vacancies, both of which critically influence the optical and magnetic properties. These results highlight the importance of defect engineering and local structural modulation in tuning the multifunctional properties of $LaFeO_3$-based perovskites.

Keywords: $LaFeO_3$, Magnetism, Bandgap, Hybridization, Local Structure

I. Introduction

Perovskite-type oxides, particularly rare-earth orthoferrites of the general formula $RFeO_3$ (where R is a rare earth element), have garnered significant attention due to their intriguing magnetic, electrical, and catalytic properties. Among them, $LaFeO_3$ stands out as a G-type antiferromagnetic insulator with a high Néel temperature (~740 K) and orthorhombic distortion arising from tilted FeO_6 octahedra.[1] Its robust magnetic ordering and thermal stability make it a promising candidate for a wide range of applications, including magnetic sensors,[2] spintronics,[3] and solid oxide fuel cells.[4] In recent years, efforts to tailor the magnetic and electronic properties of $LaFeO_3$ have focused on cationic substitution at either the A- or B-site of the perovskite lattice.[5, 6] The divalent cations Mg^{2+} are used as a substituent at both A and B sites in $LaFeO_3$ to tune the structural, optical, dielectric, and magnetic properties.[7-9] Mg^{2+}-substitution at Fe^{3+} sites in $LaFeO_3$ single phase nanoparticle alters the structure and optical properties at room temperature[7] by increasing oxygen vacancy concentration which reduces the optical bandgap of $LaFeO_3$ nanoparticles. Lin *et al*. have demonstrated that Mg^{2+}-doped $LaFeO_3$ samples exhibit a perovskite orthorhombic structure (space group *Pnma*), with optimal phase purity and magnetic properties achieved at a calcination temperature of 600 °C.[8] Increasing Mg^{2+} content in $LaFeO_3$ enhances saturation magnetization but decreases coercivity, while higher calcination temperatures (800–1000 °C) lead to the formation of impurity phases like $MgFe_2O_4$, affecting both structure and magnetism. Mg^{2+}-doped $LaFeO_3$ ($LaFe_{2/3}Mg_{1/3}O_3$) synthesized via the sol–gel method showed a significantly enhanced infrared emissivity of 0.93 in the 0.2–2 μm range - 121% higher than undoped $LaFeO_3$.[10] This improvement is due to Mg^{2+} substitution introducing Fe^{4+} impurities, oxygen vacancies, and lattice distortions, which enhance absorption through impurity levels, lattice vibrations, and polaron hopping.

In this study, a series of $LaFeO_3$ based ceramics were synthesized, including pristine $LaFeO_3$, Mg^{2+}-incorporated La-deficient $LaFeO_3$ ($La_{1-x}FeO_{3-\delta}$; xMg, x = 0.2, 0.4) and Fe-deficient $LaFeO_3$ ($LaFe_{1-x}O_{3-\delta}$; xMg, x = 0.2, 0.4). The incorporation of divalent Mg^{2+} ions at La^{3+} and Fe^{3+} sites introduced oxygen vacancies and minor secondary phases. Optical and magnetic properties varied significantly with the substitution site. Mg^{2+} incorporation in La-deficient samples led to a clear absorption edge with a reduced bandgap (2.2 to 2.3 eV), while the Fe-deficient counterparts exhibited broad absorption indicative of mid-gap defect states. Magnetically, La-deficient Mg-doped samples showed substantial increase in saturation magnetization (6-11×) and a tenfold reduction in coercivity, suggesting emergent ferromagnetic behavior. In contrast, Fe-deficient Mg-doped $LaFeO_3$ exhibited only weak magnetization enhancement (1.3-1.7×). Structural and spectroscopic analyses confirmed site-specific Mg^{2+} substitution at La^{3+} sites in La-deficient and at Fe^{3+} sites in Fe-deficient samples. Electronic structure analysis further reveals modified hybridization between Fe(3*d*)-O(2*p*), La(5*d*)-O(2*p*), Fe(4*sp*)-O(2*p*) orbitals, without changes in cation oxidation states. These results demonstrate the critical role of cation site selectivity and defect engineering in tuning the optical and magnetic properties of $LaFeO_3$-based perovskites.

II. Experimental

Pristine $LaFeO_3$, Mg^{2+}-incorporated La-deficient $LaFeO_3$ ($La_{1-x}FeO_{3-\delta}$; xMg, x = 0.2 and 0.4) and Fe-deficient $LaFeO_3$ ($LaFe_{1-x}O_{3-\delta}$; xMg, x = 0.2 and 0.4) ceramics were synthesized using low temperature citrate sol-gel method. The synthesis procedure for pristine $LaFeO_3$ nanoparticles has been described in our earlier report.[11] To prepare $La_{1-x}FeO_{3-\delta}$:xMg and $LaFe_{1-x}O_{3-\delta}$:xMg (x = 0.2 and 0.4) nanoparticles, stoichiometric amounts of $Mg(NO_3)_2.6H_2O$ were dissolved in deionized water along with the respective La and Fe precursors. Identical annealing and sintering procedures were employed to obtain the final nanoparticle powders and ceramic pellets.

X-ray diffraction measurements were conducted to examine the phase formation and crystallinity of pristine $LaFeO_3$, Mg^{2+}-incorporated La-deficient $LaFeO_3$ and Fe-deficient $LaFeO_3$ ceramics. The measurements were performed using a Rigaku diffractometer with Cu-K_α radiation (1.5406 Å). Raman spectra were recorded using Horiba Jobin Yvon HR800UV micro-Raman spectrometer equipped with a 632 nm He-Ne laser. Field emission scanning electron microscopy (FESEM) and energy dispersive X-ray spectroscopy (EDS) analyses were carried out using an FEI Inspect F microscope. Diffuse reflection spectroscopy was performed using a Bentham PVE300 spectrometer, equipped with an integrating sphere and a monochromatic light source. Resistivity measurements were conducted in the 10–300 K temperature range using a two-probe configuration. An Agilent Keysight B2987B electrometer was used in combination with a Lakeshore Model 335 temperature controller and a closed-cycle helium refrigerator from Sumitomo Cryogenics of America Inc. Magnetic properties were investigated using a superconducting quantum interference device (SQUID) vibrating sample magnetometer. Magnetization (M) as a function of magnetic field (H) and temperature (T) was measured. M–H hysteresis loops were recorded by sweeping magnetic field up to ±7 T. M–T curves were measured under an applied field of 500 Oe in both zero-field-cooled (ZFC) and field-cooled (FC) modes. Near-edge X-ray absorption fine structure (NEXAFS) measurements at the La $M_{4,5}$, Fe $L_{2,3}$, and O K edges were carried out at the 10D XAS-KIST beamline of the Pohang Accelerator Laboratory (PAL). All measurements were performed at room temperature under ultrahigh vacuum conditions ($\sim 10^{-9}$ Torr) using the total electron yield (TEY) mode. Deconvolution of the Fe $L_{2,3}$ and O K edge spectra was performed using PeakFit software, applying a mixed Gaussian and Lorentzian area fitting profile. X-ray absorption fine structure (XAFS) measurements at the La L_3-edge and Fe K-edges were conducted at room temperature in fluorescence mode at 1D XAS-PAL beamline and P64 Advanced XAFS beamline, PETRA III, DESY.[12] A Si (111) double-crystal monochromator with an energy resolution of $\Delta E/E \sim 10^{-4}$ was employed. The collected XAFS data were processed and normalized using the Athena software.[13] Extended X-ray absorption fine structure (EXAFS) analysis of the Fe K-edge was conducted using the Artemis program.[13]

III. Results and Discussion

A. Characterization with XRD, Raman, FESEM and EDS

Room temperature X-ray diffraction (XRD) measurements were performed to confirm the phase formation of pristine $LaFeO_3$, Mg^{2+}-incorporated La-deficient $LaFeO_3$ ($La_{1-x}FeO_{3-\delta}$: xMg, x = 0.2 and 0.4) and Fe deficient $LaFeO_3$ ($LaFe_{1-x}O_{3-\delta}$; xMg, x = 0.2 and 0.4) ceramics. Lattice parameters were determined through Rietveld refinement using a standard structural model for $LaFeO_3$ (JCPDS 74-2203), corresponding to the orthorhombic Pbnm space group. Figure 1 shows the experimental XRD patterns along with the fitted profiles obtained from the refinement. The refined lattice parameters for all compositions are summarized in Table 1. Pristine $LaFeO_3$ ceramics exhibit the diffraction peaks consistent with the orthorhombic $LaFeO_3$ structure, with no indication of any secondary phases. $La_{0.8}FeO_{3-\delta}$:0.2Mg also displays a single-phase $LaFeO_3$ structure. However, increasing the Mg^{2+} content to x = 0.4 ($La_{0.6}FeO_{3-\delta}$:0.4Mg) results in appearance of additional diffraction peaks at 35.6° and 62.5°, corresponding to the (311) and (440) planes of γ-Fe_2O_3 and $MgFe_2O_4$ phases, respectively.[8, 14] Similarly, $LaFe_{0.8}O_{3-\delta}$:0.2Mg ceramics remains phase pure, but further Mg^{2+} incorporation in $LaFe_{0.6}O_{3-\delta}$:0.4Mg leads to an additional diffraction peak at 30°, associated with the (101) plane of La_2O_3.[15] Pristine $LaFeO_3$ ceramics shows strongest diffraction peak at $2\theta \sim 32.3°$, corresponding to the (121) plane.

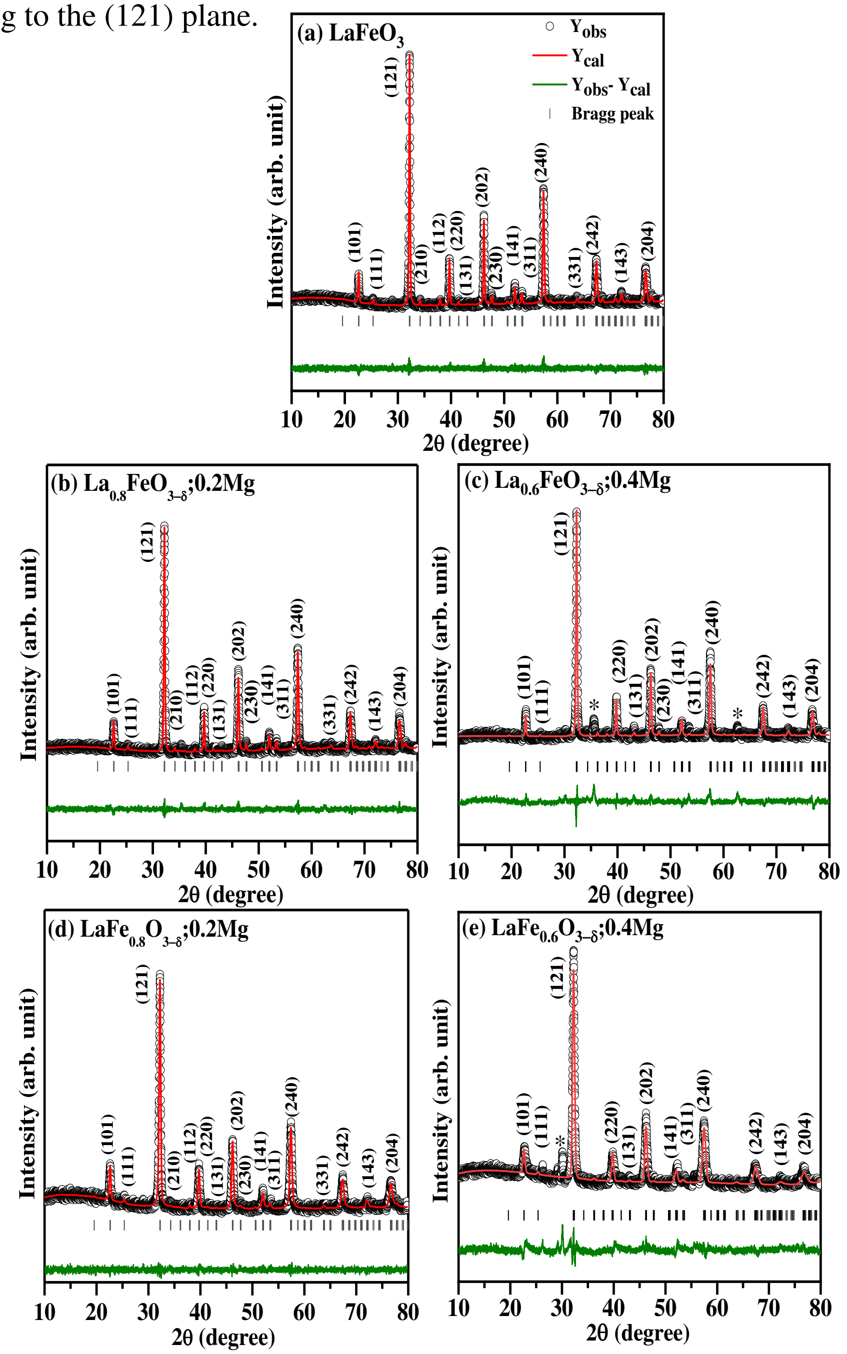

Fig. 1: *X-ray diffraction (XRD) patterns of (a) pristine $LaFeO_3$, (b, c) Mg^{2+} substituted La deficient $LaFeO_3$ ($La_{1-x}FeO_{3-\delta}$; xMg, x = 0.2 and 0.4) (d, e) Mg^{2+} substituted Fe deficient $LaFeO_3$ ($LaFe_{1-x}O_{3-\delta}$; xMg, x = 0.2 and 0.4) ceramics. Open symbol and the solid line represent the experimental data and Rietveld refinement fitting respectively. The short vertical lines below XRD pattern show the diffraction peaks. The difference between the experimental and fitted curves is shown by a horizontal line at the bottom of each diagram. Secondary phases are shown by * symbol in (c) γ-Fe_2O_3/$MgFe_2O_4$ and (e) La_2O_3.*

Table 1: *Lattice parameters and R factors of pristine* $LaFeO_3$*,* Mg^{2+} *substituted La deficient* $LaFeO_3$ *(*$La_{1-x}FeO_{3-\delta}$*; xMg, x = 0.2 and 0.4) and Fe deficient* $LaFeO_3$ *(*$LaFe_{1-x}O_{3-\delta}$*; xMg, x = 0.2 and 0.4) ceramics.*

Lanthanum orthoferrite ceramics	Lattice parameters				Average crystallite size (nm)	R-factors		
	a (Å)	b (Å)	c (Å)	V (Å^3)		R_p (%)	R_{wp} (%)	χ^2
$LaFeO_3$	5.5575(6)	5.5676(8)	7.8545(8)	242.9757(5)	42	4.71	6.00	1.20
$La_{0.8}FeO_{3-\delta}$;0.2Mg	5.5597(5)	5.5665(4)	7.8565(3)	243.1486(7)	40	4.38	5.57	1.21
$La_{0.6}FeO_{3-\delta}$;0.4Mg	5.5532(6)	5.5383(5)	7.8518(7)	241.4839(6)	48	5.68	7.54	2.70
$LaFe_{0.8}O_{3-\delta}$;0.2Mg	5.5565(6)	5.5526(5)	7.8647(4)	242.8685(7)	32	6.48	5.07	1.12
$LaFe_{0.6}O_{3-\delta}$;0.4Mg	5.5333(4)	5.5643(5)	7.8639(7)	242.1191(6)	46	6.92	9.05	2.45

This peak is observed at similar position in the $La_{1-x}FeO_{3-\delta}:x$Mg ceramics, while in the $LaFe_{1-x}O_{3-\delta}:x$Mg compositions, this peak appears broadened and slightly shifted at 2θ~32.4° (Fig. S1, Supplementary Material). The variations in the lattice parameters (*a*, *b*, *c*) and unit cell volume are presented in Fig. S2 (Supplementary Material). Both $La_{1-x}FeO_{3-\delta}:x$Mg and $LaFe_{1-x}O_{3-\delta}:x$Mg ceramics exhibit a decreasing trend in lattice parameters and unit cell volume with increasing Mg^{2+} content. These changes are likely due to lattice distortions introduced by substitution of Mg^{2+} (ionic radius ~86 pm) for La^{3+} (117 pm) and Fe^{3+} (65 pm) ions. It has been reported that higher levels of substitution lead to the formation of oxygen vacancies (V_O) into the system and the oxidation of Fe^{3+} to Fe^{4+} to maintain the charge neutrality.[16, 17] Crystallite sizes, estimated from William-Hall plots (Fig. S3 in supplementary material), are found to be in the range of 30-50 nm.

Raman spectroscopy was performed on pristine $LaFeO_3$, Mg^{2+}-incorporated La-deficient $LaFeO_3$ ($La_{1-x}FeO_{3-\delta}:x$Mg, x = 0.2 and 0.4) and Fe-deficient $LaFeO_3$ ($LaFe_{1-x}O_{3-\delta}:x$Mg, x = 0.2 and 0.4) ceramics to investigate their structural features and phase purity. According to group theoretical analysis, the *Pbnm* space group exhibits the following lattice vibrational modes:

$$\Gamma = 7A_g + 7B_{1g} + 5B_{2g} + 5B_{3g} + 8A_u + 10B_{1u} + 8B_{2u} + 10B_{3u}$$

Among these, 24 modes - specifically $\Gamma = 7A_g + 7B_{1g} + 5B_{2g} + 5B_{3g}$ are Raman active.[18] Figure 2 shows the Raman spectra of pristine $LaFeO_3$, $La_{1-x}FeO_{3-\delta}$:xMg and $LaFe_{1-x}O_{3-\delta}$:xMg; (x = 0.2 and 0.4) ceramics. The pristine $LaFeO_3$ ceramic exhibits intense Raman peaks at 141, 160, 183, 416 and 434 cm^{-1} along with moderate Raman peaks at 269, 298, 315, 336, and 629 cm^{-1}.

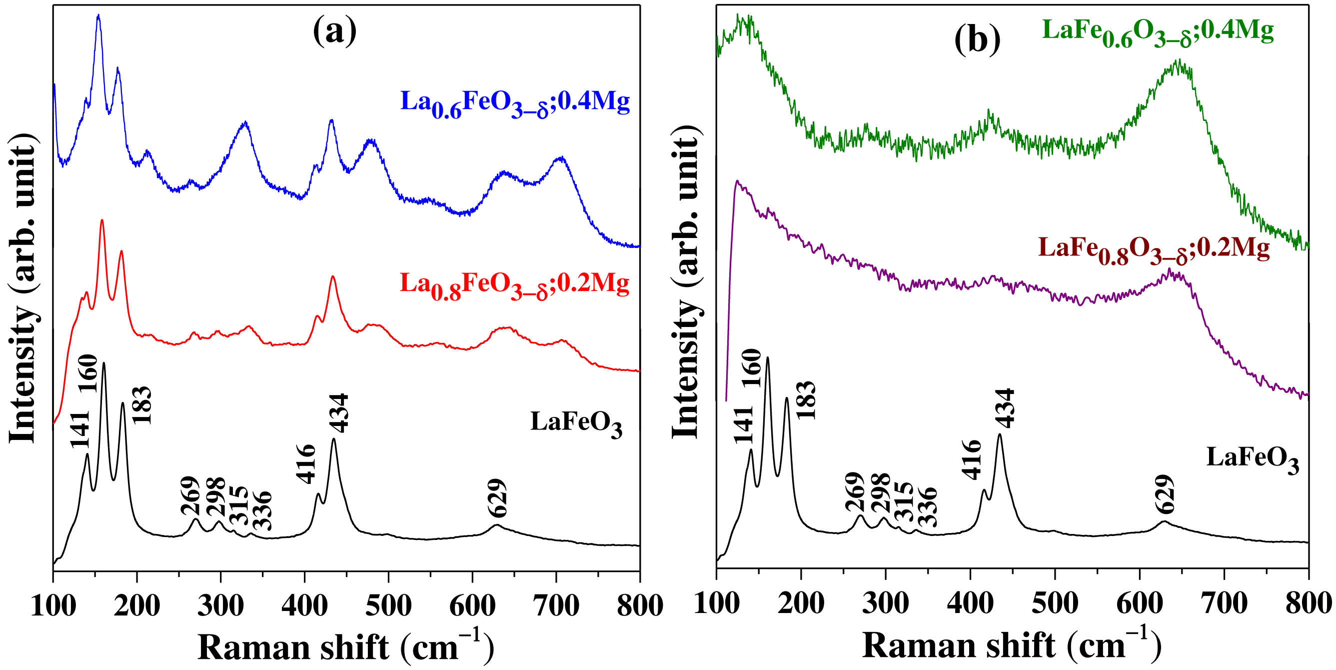

Fig. 2: *Raman spectra of pristine $LaFeO_3$ with Mg^{2+} substituted (a) La deficient $LaFeO_3$ ($La_{1-x}FeO_{3-\delta}$; xMg, x = 0.2 and 0.4) and (b) Fe deficient $LaFeO_3$ ($LaFe_{1-x}O_{3-\delta}$; xMg, x = 0.2 and 0.4) ceramics.*

The Raman spectrum can be categorized in three regions: (i) below 200 cm^{-1} – associated with La vibrations, (ii) 200 to 300 cm^{-1} - due to combined La vibrations and octahedral tilting of oxygen, and (iii) above 300 cm^{-1} – attributed to bending and stretching vibrations of FeO_6 octahedra. The $La_{0.8}FeO_{3-\delta}$:0.2Mg sample show additional, low intense broader peaks at 212, 333, 485, 638 and 707 cm^{-1}, in addition to the modes observed for pristine $LaFeO_3$. These peaks become significantly more intense in $La_{0.6}FeO_{3-\delta}$:0.4Mg, indicating enhanced structural disorder. The additional modes are attributed to oxygen non-stoichiometry, increase oxygen octahedral tilt distortion, and the presence of secondary phases such as $MgFe_2O_4$.[7, 19] In contrast, the Raman spectra of Fe-deficient $LaFeO_3$ ceramics display a broad and intense peak at 646 cm^{-1}, with no other discernible Raman-active modes. This featureless spectrum is attributed to the conducting nature of these ceramic samples, which results in suppression of Raman activity. The broad intense peak at 646 cm^{-1} is associated with changes in Fe/MgO_6 octahedra within the distorted lattice structure.[7]

FESEM was employed to examine the microstructural morphology of pristine $LaFeO_3$, $La_{1-x}FeO_{3-\delta}:x$Mg and $LaFe_{1-x}O_{3-\delta}:x$Mg (x = 0.2 and 0.4) ceramics. The images were obtained from the fractured surfaces of sintered pellets, as shown in Fig. 3. The corresponding particle size distributions are shown in the insets. Pristine $LaFeO_3$ exhibits an average particle size of approximately 90 nm. In comparison, both $La_{1-x}FeO_{3-\delta}:x$Mg and $LaFe_{1-x}O_{3-\delta}:x$Mg ceramics show increased particle agglomeration, with particle sizes ranging from 60 to 140 nm. However, no significant change in the average particle size is observed relative to pristine $LaFeO_3$. EDS spectra was performed to understand the elemental composition in pristine $LaFeO_3$, $La_{1-x}FeO_{3-\delta}$; xMg and $LaFe_{1-x}O_{3-\delta}$; xMg ceramics. The estimated atomic percentages of La, Mg, Fe, and O are summarized in Table 2, and the corresponding EDS spectra are shown in Fig. S4 (Supplementary Material). The elemental composition of $LaFeO_3$ ceramics is consistent with the nominal stoichiometry within the expected error range associated with the EDS detection limits. In contrast, both $La_{1-x}FeO_{3-\delta}:x$Mg and $LaFe_{1-x}O_{3-\delta}:x$Mg ceramics exhibit a noticeable deficiency in oxygen atomic percentage, indicative of oxygen non-stoichiometry introduced by Mg^{2+} substitution.

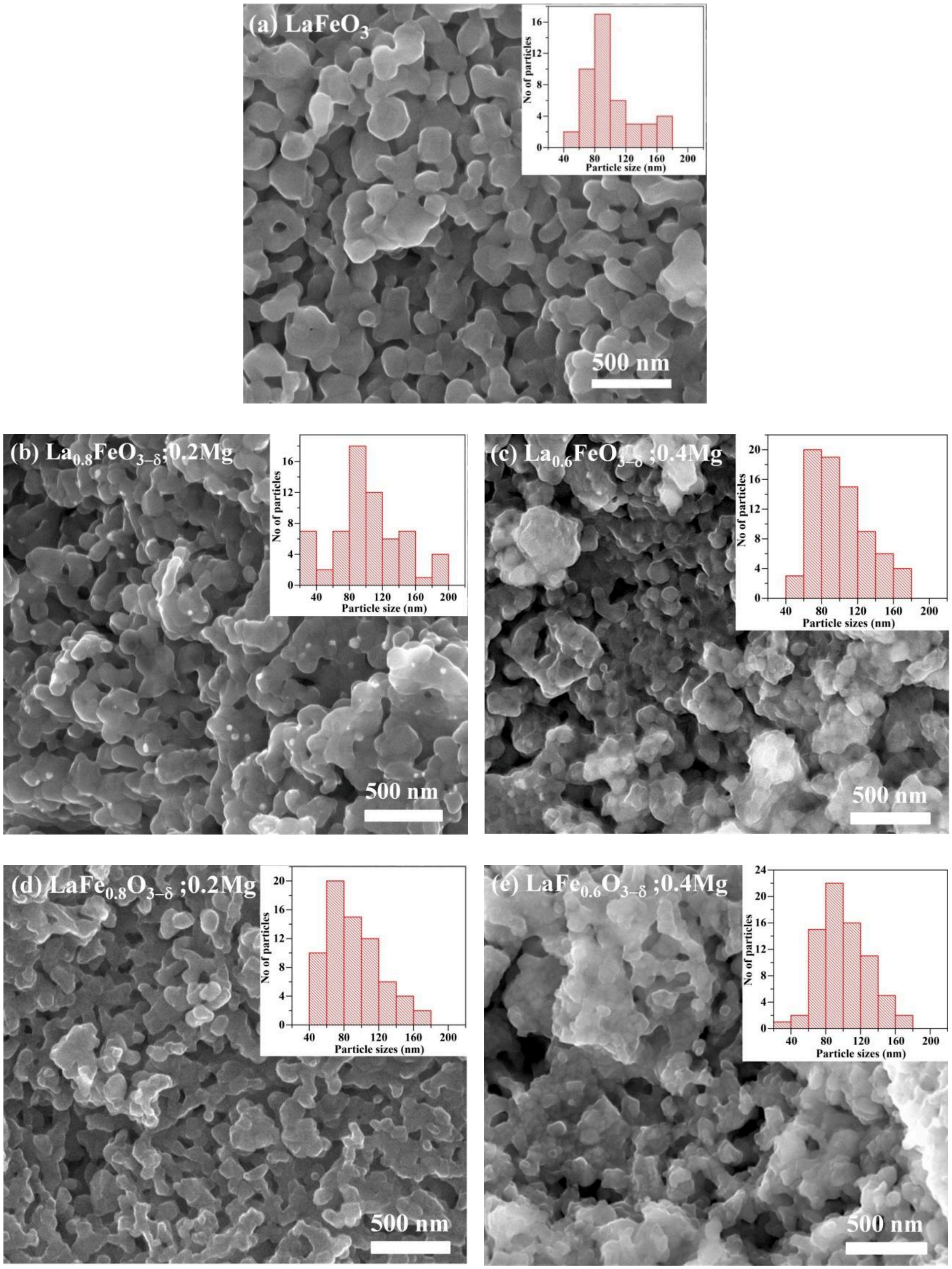

Fig. 3: *FESEM images of (a) pristine* $LaFeO_3$ *with* Mg^{2+} *substituted (b, c) La deficient* $LaFeO_3$ *(*$La_{1-x}FeO_{3-\delta}$*; xMg, x = 0.2 and 0.4) and (d, e) Fe deficient* $LaFeO_3$ *(*$LaFe_{1-x}O_{3-\delta}$*; xMg, x = 0.2 and 0.4) ceramics.*

Table 2: *Atomic percentage (at %) of the elements in pristine* $LaFeO_3$*,* Mg^{2+} *substituted La deficient* $LaFeO_3$ *(*$La_{1-x}FeO_{3-\delta}$*; xMg, x = 0.2 and 0.4) and Fe deficient* $LaFeO_3$ *(*$LaFe_{1-x}O_{3-\delta}$*; xMg, x = 0.2 and 0.4) ceramics.*

Lanthanum orthoferrite ceramics	Elements			
	La Lα	Mg Kα	Fe Kα	O Kα
	at. %	*at.%*	*at.%*	*at.%*
$LaFeO_3$	23.7	-	22.5	53.8
$La_{0.8}Mg_{0.2}FeO_{3-\delta}$	22.2	7.3	26.0	44.6
$La_{0.6}Mg_{0.4}FeO_{3-\delta}$	20.6	11.8	30.6	37.0
$LaFe_{0.8}Mg_{0.2}O_{3-\delta}$	31.6	6.6	23.7	38.2
$LaFe_{0.6}Mg_{0.4}O_{3-\delta}$	32.6	12.1	18.4	36.8

B. Macroscopic properties: Reflection (bandgap), resistivity and magnetization

The diffuse reflection spectra of pristine $LaFeO_3$, $La_{1-x}FeO_{3-\delta}:x$Mg, and $LaFe_{1-x}O_{3-\delta}:x$Mg ($x = 0.2$ and 0.4) ceramics are presented in Figs. 4a and b, respectively. Pristine $LaFeO_3$ exhibits a maximum reflectance of 38% at energy of 2.1 eV. This reflectance sharply drops to 21% in the ranges of 2.1 and 2.3 eV, indicating strong photon absorption in this energy region. The reflection of pristine $LaFeO_3$ ceramics further decrease to 17% between 2.3 and 2.6 eV attributed to photon absorption by mid-bandgap defect states. $La_{0.8}FeO_{3-\delta}$:0.2Mg ceramics show an initial reflectance of 25% at 2 eV, which gradually decreases to 16% at 2.6 eV. The reduced and gradually decaying reflectance indicates enhanced photon absorption compared to pristine $LaFeO_3$, due to the presence of mid-bandgap V_O defect states. Similarly, $La_{0.6}FeO_{3-\delta}$:0.4Mg ceramics exhibit a reflectance of 28% at 2 eV, decreasing to 15% at 2.6 eV with increasing Mg^{2+} content. In contrast, $LaFe_{0.8}O_{3-\delta}$:0.2Mg and $LaFe_{0.6}O_{3-\delta}$:0.4Mg ceramics show nearly flat reflectance curves in the 2-3 eV range, maintaining values between 12% and 14%. This behavior suggests that most incident photons are absorbed, consistent with the formation of dense and continuous mid-bandgap V_O defects. To estimate the optical bandgap (E_g), Tauc plots were derived from diffuse reflectance (R) spectra using the Kubelka-Munk function, $[F(R) = \frac{(1-R)^2}{2R}]$, as shown in Figs. 4c and 4d. The bandgap (E_g) was obtained using Tauc's equation $(\alpha h\nu)^2 = C(h\nu - E_g)$; where F(R) is approximated as the absorption coefficient (α).

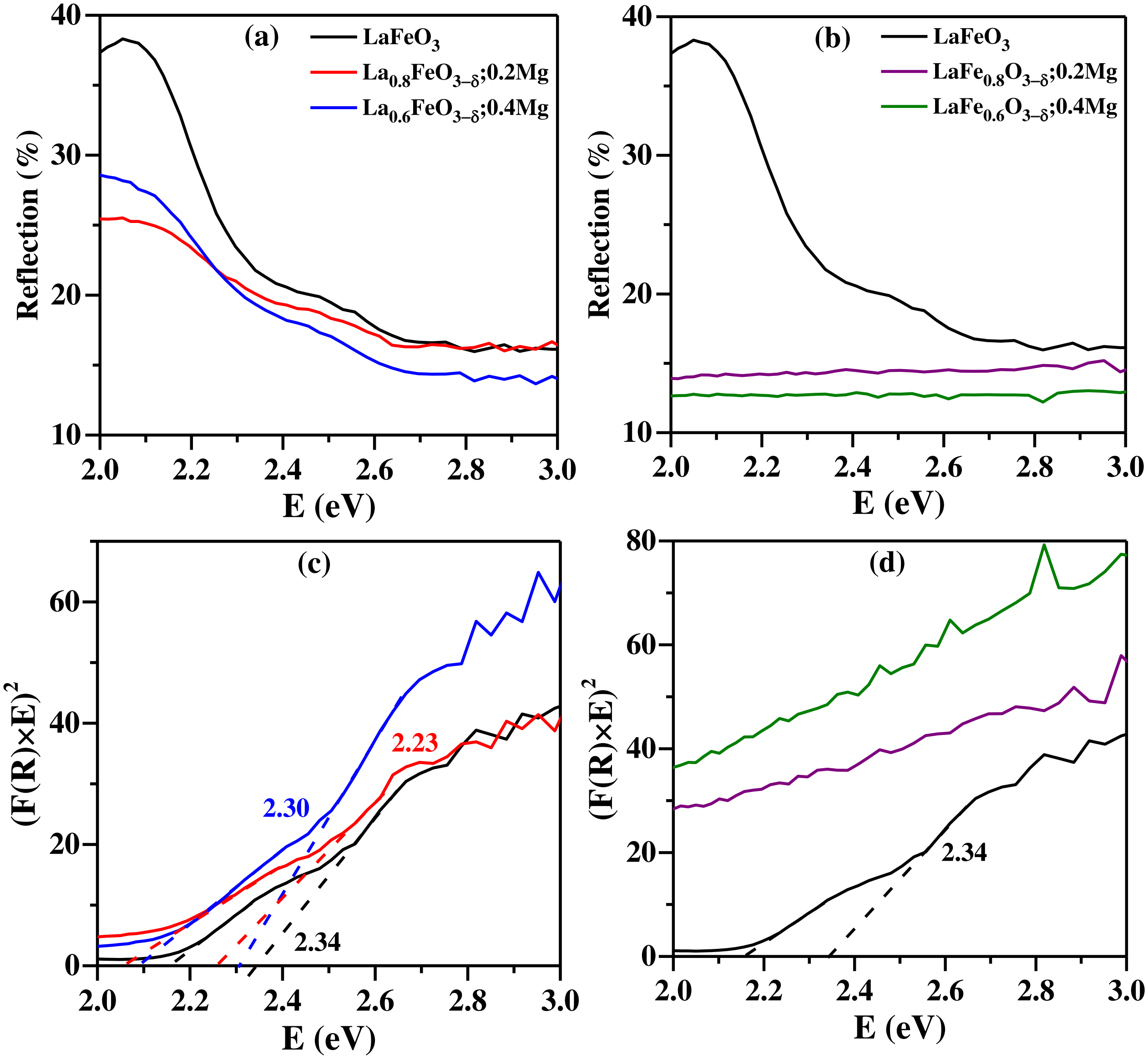

Fig. 4: *(a, b) Diffuse reflection and (c, d) Tauc plot using Kubelka-Munk function F(R) of pristine* $LaFeO_3$ *with* Mg^{2+} *substituted (a, c) La deficient* $LaFeO_3$ *(*$La_{1-x}FeO_{3-\delta}$*; xMg, x = 0.2 and 0.4) and (b, d) Fe deficient* $LaFeO_3$ *(*$LaFe_{1-x}O_{3-\delta}$*; xMg, x = 0.2 and 0.4) ceramics.*

For pristine $LaFeO_3$, the bandgap is estimated to be 2.34 eV, corresponding to the charge transfer between O 2*p* and Fe 3*d* states. The bandgap values decrease to 2.23 and 2.30 eV for

$La_{0.8}FeO_{3-\delta}$:0.2Mg and $La_{0.6}FeO_{3-\delta}$:0.4Mg, respectively indicates the formation of mid-bandgap states due to V_O defects. These defects, located near the conduction band, give rise to additional band edge at lower energies - 2.16, 2.05 and 2.08 eV for pristine $LaFeO_3$, $La_{0.8}FeO_{3-\delta}$:0.2Mg and $La_{0.6}FeO_{3-\delta}$:0.4Mg, respectively. Conversely, $LaFe_{0.8}O_{3-\delta}$:0.2Mg and $LaFe_{0.6}O_{3-\delta}$:0.4Mg ceramics exhibit continuously decreasing spectra without a distinct band edge, confirming the existence of broad and dense distribution of mid-gap V_O defect states between valence and conduction bands. These results suggest that Mg^{2+} substitution in La-deficient $LaFeO_3$ promotes the formation of moderate V_O related mid-bandgap defect states, whereas Mg^{2+} incorporation in Fe deficient $LaFeO_3$ leads to the development of dense and continuous V_O mid-bandgap defect states.

Temperature dependent resistivity measurements were carried out on pristine $LaFeO_3$, $La_{1-x}FeO_{3-\delta}$:xMg and $LaFe_{1-x}O_{3-\delta}$:xMg (x = 0.2 and 0.4) ceramics to understand the electrical behavior. These measurements were performed using the two-probe method in the temperature range of 10-300 K (Fig. 5). At room temperature, pristine $LaFeO_3$ exhibits a resistivity of 10^8 Ω.cm, whereas $La_{0.8}FeO_{3-\delta}$:0.2Mg (10^9 Ω.cm) and $La_{0.6}FeO_{3-\delta}$:0.4Mg (2×10^{10} Ω.cm) show an increase in resistivity by one to two orders of magnitude compared to pristine $LaFeO_3$ (Fig. 5a). Upon cooling, the resistivity increases to 4×10^9 Ω.cm at 170 K, below which it decreases slightly. In contrast, $La_{0.8}FeO_{3-\delta}$:0.2Mg and $La_{0.6}FeO_{3-\delta}$:0.4Mg ceramics exhibit a sharp increase in resistivity with decreasing temperature, reaching 8×10^{11} Ω.cm at 214 K and 10^{13} Ω.cm at 274 K, respectively. Similarly, $LaFe_{0.8}O_{3-\delta}$:0.2Mg and $LaFe_{0.6}O_{3-\delta}$:0.4Mg ceramics display resistivity values of 3×10^{10} Ω.cm and 3×10^8 Ω.cm, respectively, at room temperature, which increase sharply to 3×10^{13} Ω.cm at 270 K and 10^{13} Ω.cm at 190 K. Notably, no abrupt change in resistivity is observed across the temperature range that would indicate a phase transition.

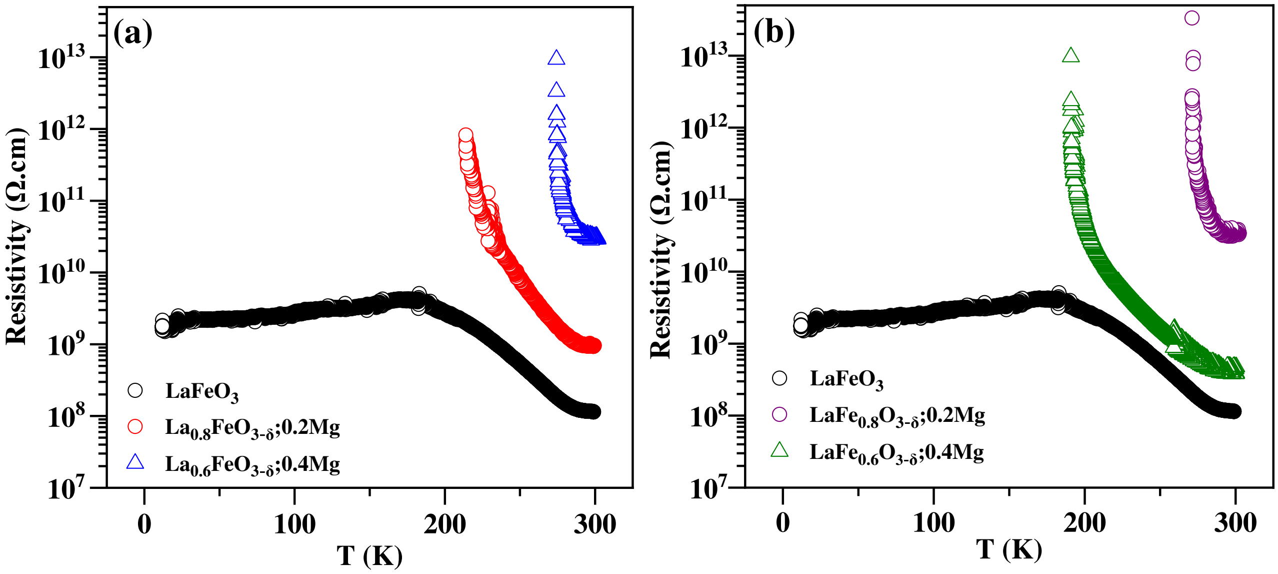

Fig. 5: *Resistivity of pristine* $LaFeO_3$ *with* Mg^{2+} *substituted (a) La deficient* $LaFeO_3$ *(*$La_{1-x}FeO_{3-\delta}$*; xMg, x = 0.2 and 0.4) and (b) Fe deficient* $LaFeO_3$ *(*$LaFe_{1-x}O_{3-\delta}$*; xMg, x = 0.2 and 0.4) ceramics.*

Magnetic field dependent magnetization (M-H curve) measurements were conducted on pristine $LaFeO_3$, $La_{1-x}FeO_{3-\delta}$:xMg and $LaFe_{1-x}O_{3-\delta}$:xMg (x = 0.2 and 0.4) ceramics to study the magnetic properties. The M-H curves measured at 5 K and 300 K are shown in Fig. 6. Pristine $LaFeO_3$ and $LaFe_{1-x}O_{3-\delta}$:xMg (x = 0.2 and 0.4) ceramics exhibit weak ferromagnetism, while $La_{1-x}FeO_{3-\delta}$:xMg (x = 0.2 and 0.4) ceramics show pronounced ferromagnetic behavior. The saturation magnetization (M_S), remnant magnetization (M_R), and coercivity (H_C) at 5 K and 300 K are summarized in Table 3. Pristine $LaFeO_3$ is known to be G-type antiferromagnetic due to the super exchange interactions between Fe^{3+} ions mediated by O^{2-}. It is reported that pristine $LaFeO_3$ shows weak ferromagnetism due to the net unbalanced moment produced by FeO_6 octahedral tilt along the c-axis.[20, 21] The uncompensated spin at surface of smaller crystallite size of pristine $LaFeO_3$ originates weak ferromagnetism.[20] The M_S and M_R values for pristine $LaFeO_3$ are 0.7 and 0.08 emu/g, respectively (Table 3).

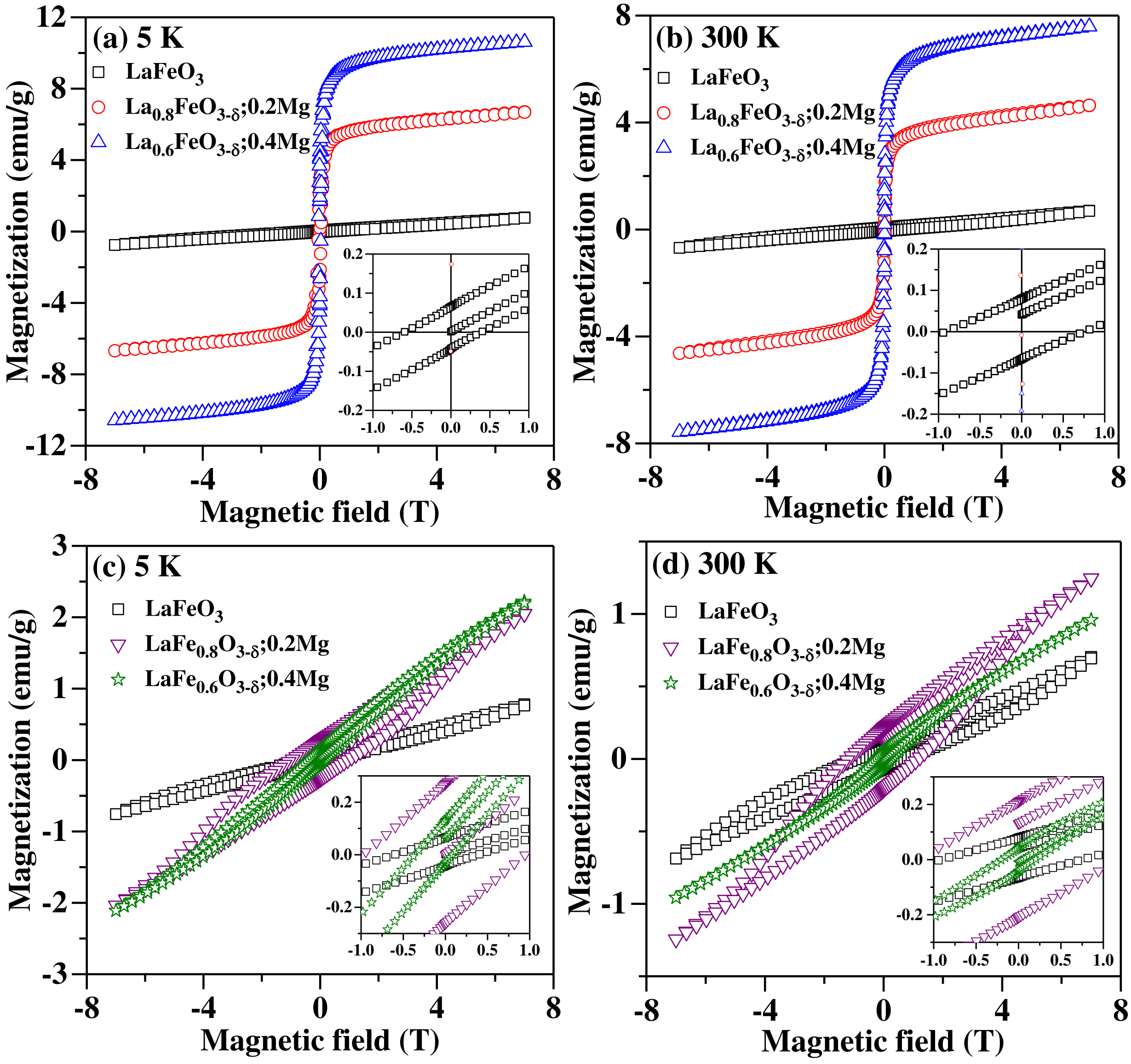

Fig. 6: *Magnetic field dependent magnetization curves at (a, c) 5 K and (b, d) 300 K for pristine* $LaFeO_3$, *with* Mg^{2+} *substituted (a, b) La deficient* $LaFeO_3$ ($La_{1-x}FeO_{3-\delta}$; *xMg, x = 0.2 and 0.4) and (c, d) Fe deficient* $LaFeO_3$ ($LaFe_{1-x}O_{3-\delta}$; *xMg, x = 0.2 and 0.4) ceramics. Insets show the magnified magnetization curve to visualize remnant magnetization and coercivity.*

Significant enhancement in M_S and M_R are observed for $La_{1-x}FeO_{3-\delta}$:xMg (x = 0.2 and 0.4) ceramics both at 5 and 300 K (Figs. 5a and b). At 300K, the M_S increases 6 to 7 times (4.6 emu/g) for $La_{0.8}FeO_{3-\delta}$;0.2Mg and by one order (7.6 emu/g) for $La_{0.6}FeO_{3-\delta}$;0.4Mg compared to 0.7 emu/g found in pristine $LaFeO_3$. Similarly, the M_R increases significantly to 0.74 and 1.52 emu/g, respectively. The coercive field (H_C) decreases from 0.9 T in pristine $LaFeO_3$ to 0.01 T in

$La_{1-x}FeO_{3-\delta}$:xMg (x = 0.2 and 0.4) samples. These changes in M_S, M_R, and H_C, found to be interesting in $La_{1-x}FeO_{3-\delta}$;xMg (x = 0.2 and 0.4) ceramics arise not only due to the formation of V_O defects created by aliovalent substitution but also from modifications in electronic structure. The formation of secondary phases like γ-Fe_2O_3/$MgFe_2O_4$ estimated at 2 to 5 *wt.%* in $La_{1-x}FeO_{3-\delta}$:xMg (x = 0.2 and 0.4) ceramics may contribute 2-3 emu/g to the total magnetization. In Mg^{2+} substituted Fe-deficient $LaFeO_3$ ceramics, M_S values of 1.2 and 0.9 emu/g are observed for x = 0.2 and 0.4, respectively – slightly higher than that of pristine $LaFeO_3$ (0.7 emu/g). This increase in M_S is primarily attributed to the V_O defects arising from aliovalent Mg^{2+} substitution in Fe deficient $LaFeO_3$. The M_R and H_C values for $LaFe_{1-x}O_{3-\delta}$:xMg (x = 0.2 and 0.4) ceramics remain similar to those of pristine $LaFeO_3$. Similar trends in M_S, M_R and H_C are seen at 5 K, with increased values due to suppressed thermal fluctuations.

Table 3: *Saturation magnetization (M_S), remnant magnetization (M_R), and coercivity (H_C) of pristine $LaFeO_3$, Mg^{2+} substituted La deficient $LaFeO_3$ ($La_{1-x}FeO_{3-\delta}$; xMg, x = 0.2 and 0.4) and Fe deficient $LaFeO_3$ ($LaFe_{1-x}O_{3-\delta}$; xMg, x = 0.2 and 0.4) ceramics.*

Lathanum Orthoferrite ceramics	M_S in emu/g		M_R in emu/g		H_C in T	
	Temperature					
	5 K	300 K	5 K	300 K	5 K	300 K
$LaFeO_3$	0.8	0.7	0.06	0.08	0.6	0.9
$La_{0.8}FeO_{3-\delta}$;0.2Mg	6.7	4.6	2.44	0.74	0.05	0.01
$La_{0.6}FeO_{3-\delta}$;0.4Mg	10.6	7.6	4.10	1.52	0.04	0.01
$LaFe_{0.8}O_{3-\delta}$;0.2Mg	2.1	1.2	0.27	0.21	1.02	1.12
$LaFe_{0.6}O_{3-\delta}$;0.4Mg	2.2	0.9	0.13	0.04	0.34	0.18

To further probe the magnetic behavior, temperature dependent magnetization measurements were carried out under zero-field-cooled (ZFC) and field-cooled (FC) conditions at 500 Oe for all compositions (Fig. 7).

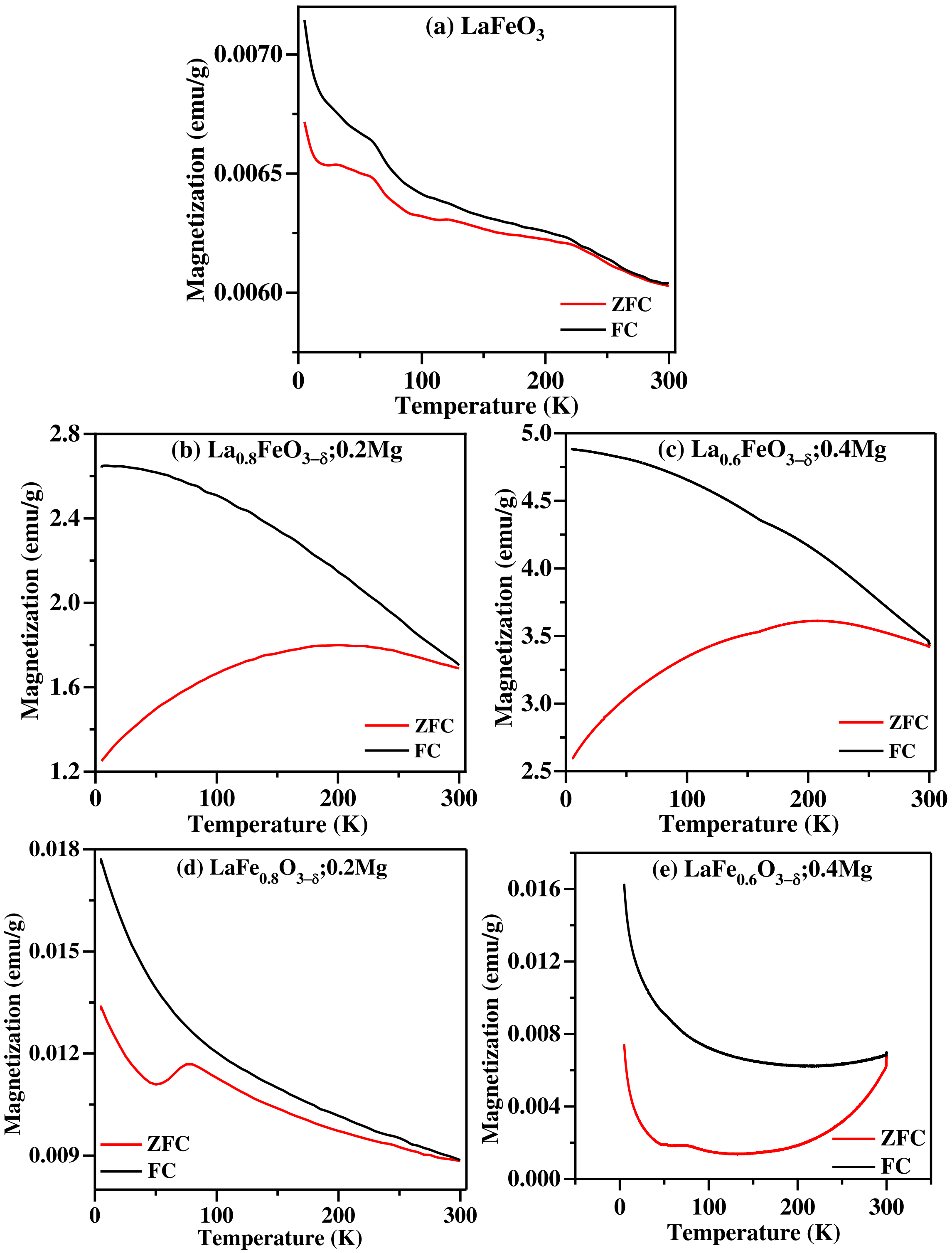

Fig. 7: *Temperature dependent magnetization of (a) pristine* $LaFeO_3$*, (b, c)* Mg^{2+} *substituted La deficient* $LaFeO_3$ *(*$La_{1-x}FeO_{3-\delta}$*; xMg, x = 0.2 and 0.4) and (d, e)* Mg^{2+} *substituted Fe deficient* $LaFeO_3$ *(*$LaFe_{1-x}O_{3-\delta}$*; xMg, x = 0.2 and 0.4) ceramics at zero field cool (ZFC) and field cool (FC) conditions.*

In pristine $LaFeO_3$, the magnetization decreases almost linearly with increasing the temperature, and the small splitting between ZFC and FC curves at lower temperature indicates weak ferromagnetism.[22] The $La_{1-x}FeO_{3-\delta}$:xMg ceramics exhibit pronounced bifurcation between ZFC and FC curves, indicating the presence of a strong ferromagnetic component in the system. Conversely, $LaFe_{1-x}O_{3-\delta}$:xMg ceramics show reduced ZFC and FC bifurcation, suggesting diminished ferromagnetic components. These results demonstrate that the temperature-dependent magnetization behavior is strongly influenced by both the nature of substituent ion and the specific substitution site. Notably, a sharp drop in magnetization is observed at ~ 88 K in ZFC curve of $LaFe_{0.8}O_{3-\delta}$:0.2Mg, which may be attributed to charge ordering associated with charge disproportion phenomena.[23]

C. Element specific characterization: NEXAFS, XANES, EXAFS

To investigate the changes in the oxidation states and electronic structure of pristine $LaFeO_3$, Mg^{2+} incorporated La-deficient $LaFeO_3$ ($La_{1-x}FeO_{3-\delta}$:xMg, x = 0.2 and 0.4) and Fe-deficient $LaFeO_3$ ($LaFe_{1-x}O_{3-\delta}$:xMg, x = 0.2 and 0.4) ceramics, NEXAFS measurements were carried out at La $M_{4,5}$–edge, Fe $L_{2,3}$-edge and O K-edge. Figure S5 shows the NEXAFS spectra of La $M_{4,5}$-edge for pristine $LaFeO_3$, $La_{1-x}FeO_{3-\delta}$:xMg and $LaFe_{1-x}O_{3-\delta}$:xMg (x = 0.2 and 0.4) ceramics. Two intense peaks at 835.8 eV and 852.0 eV are observed in pristine $LaFeO_3$, corresponding to electronic transitions from La $3d_{5/2}$ and La $3d_{3/2}$ core levels, known as M_5 and M_4 edges, respectively. These peaks appear at same energies (835.8 eV for M_5-edge and 852.0 eV for M_4-edge) in both La-deficient and Fe-deficient Mg^{2+}- incorporated compositions, indicating that the oxidation state and electronic structure of La ions remain essentially unchanged across all samples. The NEXAFS spectra of the Fe $L_{2,3}$-edge, along with their de-convoluted components, for pristine $LaFeO_3$, Mg^{2+}-incorporated La deficient (Figs. 8b, 8c) and Fe-deficient $LaFeO_3$ (Figs. 8d, 8e) are shown in Fig. 8.

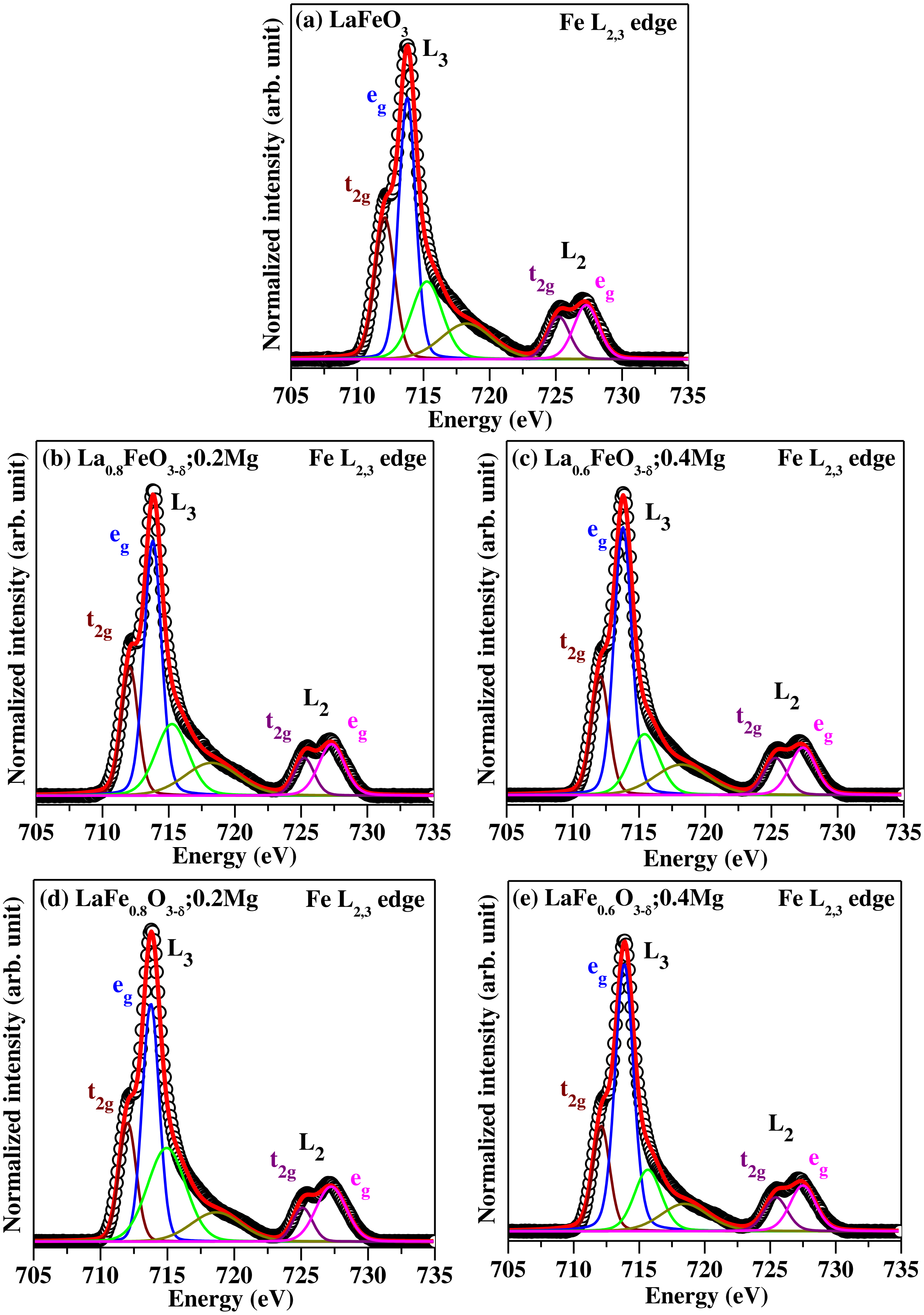

Fig. 8: *Near edge X-ray absorption fine structure (NEXAFS) spectra of Fe $L_{2,3}$-edge for (a) pristine $LaFeO_3$ with Mg^{2+} substituted (b, c) La deficient $LaFeO_3$ ($La_{1-x}FeO_{3-\delta}$; xMg, x = 0.2 and 0.4) and (d, e) Fe deficient $LaFeO_3$ ($LaFe_{1-x}O_{3-\delta}$; xMg, x = 0.2 and 0.4) ceramics.*

Fe L_3 and L_2-edges are de-convoluted into t_{2g} and e_g peaks, with the corresponding peak positions, amplitude ratios, and area ratios summarized in Table 4. In pristine $LaFeO_3$, the L_3-t_{2g} and L_3-e_g peaks appear at 712.1 eV and 713.8 eV, respectively. The energy separation of 1.7 eV between these peaks indicates Fe^{3+} oxidation states in pristine $LaFeO_3$.[24] The L_3-t_{2g} and L_3-e_g separation remains similar (1.7-1.8 eV) for all Mg^{2+} incorporated La- and Fe- deficient compositions, suggesting that the Fe oxidation state remains Fe^{3+} across all samples. However, the amplitude and area ratios of L_3-t_{2g} and L_3-e_g decrease in $La_{1-x}FeO_{3-\delta}$:xMg (x = 0.2 and 0.4) samples compared to pristine $LaFeO_3$, with a further reduction in the $LaFe_{1-x}O_{3-\delta}$:xMg (x = 0.2 and 0.4) samples. Similarly, the L_2-t_{2g} (725.2 eV) and L_2-e_g (727.3 eV) peak positions observed in pristine $LaFeO_3$ ceramic remain nearly unchanged in $La_{1-x}FeO_{3-\delta}$; xMg and $LaFe_{1-x}O_{3-\delta}$; xMg (x = 0.2 and 0.4) ceramics. Nonetheless, their amplitude and area ratios decrease in all doped samples relative to pristine compound. The error involved in determining peak position is ±0.1 eV, while total error is found to be ~5% in amplitude and area ratio.

Table 4: *Peak position, amplitude ratio, and area ratio of t_{2g} and e_g peaks for L_3 and L_2 edges of pristine $LaFeO_3$, Mg^{2+} substituted La deficient $LaFeO_3$ ($La_{1-x}FeO_{3-\delta}$; xMg, x = 0.2 and 0.4) and Fe deficient $LaFeO_3$ ($LaFe_{1-x}O_{3-\delta}$; xMg, x = 0.2 and 0.4) ceramics.*

Sample name	L_3 edge				L_2 edge			
	Peak position (eV)		Amplitude ratio	Area ratio	Peak position (eV)		Amplitude ratio	Area ratio
	t_{2g}	e_g	(t_{2g}/e_g)	(t_{2g}/e_g)	t_{2g}	e_g	(t_{2g}/e_g)	(t_{2g}/e_g)
$LaFeO_3$	712.1	713.8	0.54	0.63	725.2	727.3	0.79	0.70
$La_{0.8}FeO_{3-\delta}$;0.2Mg	712.1	713.8	0.51	0.48	725.2	727.3	0.73	0.55
$La_{0.6}FeO_{3-\delta}$;0.4Mg	712.0	713.8	0.50	0.51	725.1	727.2	0.61	0.40
$LaFe_{0.8}O_{3-\delta}$;0.2Mg	712.1	713.8	0.44	0.43	725.3	727.4	0.78	0.68
$LaFe_{0.6}O_{3-\delta}$;0.4Mg	712.1	713.9	0.39	0.37	725.4	727.5	0.74	0.67

The O K-edge NEXAFS spectra and their de-convoluted peaks for pristine $LaFeO_3$, Mg^{2+} incorporated La-deficient $LaFeO_3$ ($La_{1-x}FeO_{3-\delta}$:xMg, $x = 0.2$ and 0.4) and Fe-deficient $LaFeO_3$ ($LaFe_{1-x}O_{3-\delta}$; xMg, $x = 0.2$ and 0.4) are presented in Fig. 9. The spectra for pristine $LaFeO_3$ can be divided into three distinct energy regions. *Region I (530–534.5 eV):* This arises from the hybridization of O 2*p* and Fe 3*d* states, with two prominent peaks at 532.1 and 533.5 eV. In Mg^{2+}-incorporated La- and Fe-deficient $LaFeO_3$ compositions, the intensities of these peaks are markedly reduced, indicating a weakening of O 2*p*–Fe 3*d* hybridization. This reduction arises from Mg^{2+} substitution at La^{3+} or Fe^{3+} sites, which perturbs the local electronic environment and affects the hybridization. Additionally, a weak pre-edge feature near 530 eV appears in Fe-deficient Mg^{2+} incorporated samples, which is attributed to transitions involving defect-induced states with significant O 2*p* character, likely associated with oxygen vacancies and defect-induced states introduced by Mg^{2+} substitution at the Fe site.[24] *Region II (534.5-540.2 eV):* The O K-edge NEXAFS spectra from this region corresponds to the hybridization between O 2*p* and La 5*d* electronic states. In pristine $LaFeO_3$, two peaks of nearly equal intensity are observed at ~536.0 eV and ~538.5 eV. In $La_{0.8}FeO_{3-\delta}$:0.2Mg samples, the 536.0 eV peak becomes significantly more intense than the 538.5 eV peak, while at higher Mg^{2+} content ($x = 0.$), the intensities become more comparable, suggesting partial restoration of hybridization symmetry. In Fe-deficient compositions Mg^{2+} substituted samples ($LaFe_{1-x}O_{3-\delta}$; xMg, $x = 0.2$ and 0.4), a more pronounced intensity difference is observed, indicating a greater disruption of O 2*p*–La 5*d* hybridization due to local coordination changes and charge compensation effects. *Region 3 (540.2-552 eV)*: The O 2*p* and Fe 4*sp* hybridization displays three peaks at ~542 eV, ~545 eV, and ~547 eV in pristine $LaFeO_3$. In the La-deficient Mg^{2+}-incorporated ($La_{1-x}FeO_{3-\delta}$: xMg) and

Fe-deficient (La$Fe_{1-x}O_{3-\delta}$; xMg) compositions (x = 0.2 and 0.4), notable variations in the relative intensities are observed, reflecting modifications in O 2p–Fe 4sp hybridization.

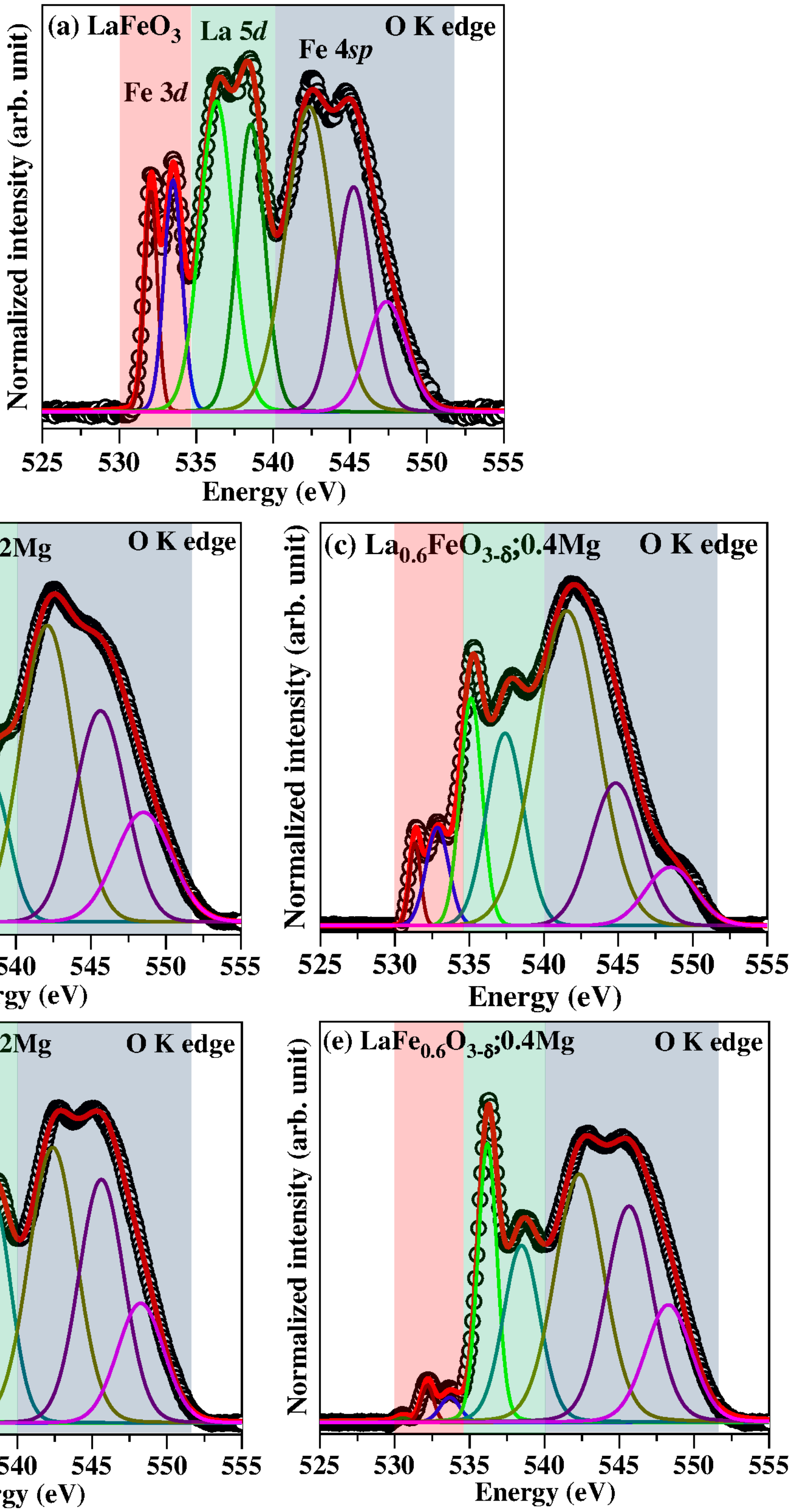

Fig. 9: *Near edge X-ray absorption fine structure (NEXAFS) spectra of O K-edge for (a) pristine* $LaFeO_3$ *with* Mg^{2+} *substituted (b, c) La deficient* $LaFeO_3$ ($La_{1-x}FeO_{3-\delta}$; *xMg, x = 0.2 and 0.4) and (d, e) Fe deficient* $LaFeO_3$ ($LaFe_{1-x}O_{3-\delta}$; *xMg, x = 0.2 and 0.4) ceramics.*

Mg^{2+} substitution introduces local structural and electronic distortions due to its higher electron affinity, perturbing the hybridization not only in the O 2*p*–Fe 4*sp* channel but also O 2*p*–Fe 3*d* and O 2*p*–La 5*d* interactions. This demonstrates the broad impact of Mg^{2+} incorporation on the electronic structure of the $LaFeO_3$ matrix.

X-ray absorption near edge structure (XANES) studies at the La L_3-edge and Fe K-edge were carried out to determine the oxidation states of La and Fe in pristine $LaFeO_3$, Mg^{2+}-incorporated La-deficient $LaFeO_3$ ($La_{1-x}FeO_{3-\delta}$:xMg, x = 0.2 and 0.4) and Fe deficient $LaFeO_3$ ($LaFe_{1-x}O_{3-\delta}$:xMg, x = 0.2 and 0.4) ceramics. The normalized La L_3-edge XANES spectra for these ceramics are shown in Fig. 10a. All spectra exhibit a peak at 5484.5 eV, indicating similar La oxidation states. The white-line region, highlighted in the inset of Fig. 10a, shows increased area in both La-deficient and Fe-deficient Mg^{2+} incorporated samples compared to pristine $LaFeO_3$. This change in the white line area correlates with variations in lattice parameters and cell volume due to Mg^{2+} incorporation. The increase is more pronounced in La deficient compositions than in Fe deficient ones. To determine the main absorption edge, the first derivative of the normalized XANES spectra is plotted (Fig. 10b). A strong peak at ~5480 eV is observed for all samples, confirming no shift in the absorption edge and indicating that La remains in the 3+ oxidation states (La^{3+}) across all compositions. Similarly, the normalized Fe K-edge XANES spectra and their first derivatives are shown Figs. 10c and 10d. The insets in Fig. 10c highlight the pre-peak and white-line regions. All samples show a main peak at 7129 eV, while La-deficient Mg^{2+}-incorporated samples additionally display a small pre-peak at 7113 eV. The white-line area of Fe-deficient Mg^{2+}-incorporated $LaFeO_3$ samples is comparable to pristine

$LaFeO_3$, whereas La-deficient Mg^{2+}-incorporated $LaFeO_3$ samples show a reduced white line area.

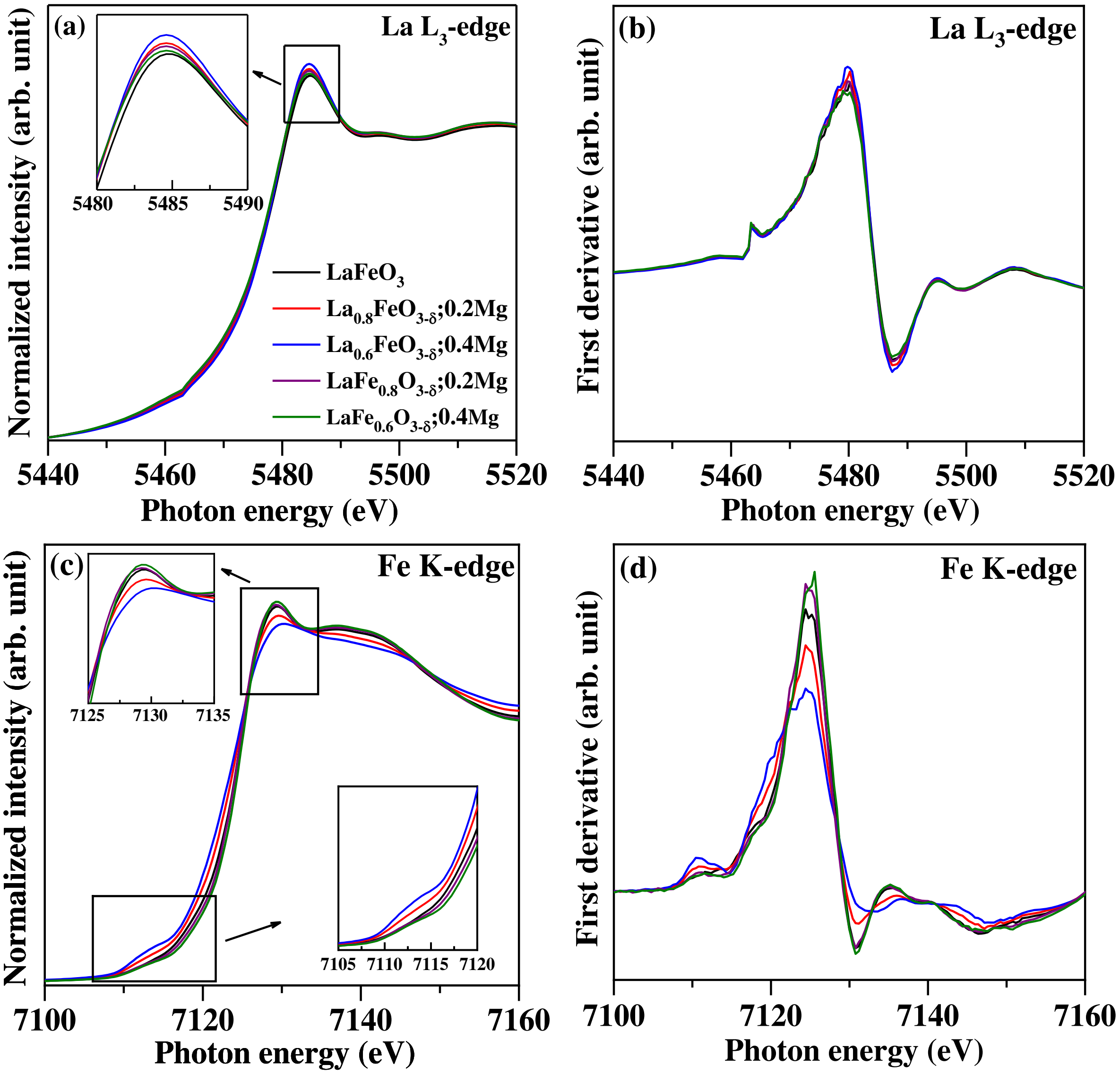

Fig. 10: *(a, b) La L_3-edge and (c, d) Fe K-edge (a, c) normalized and (b, d) first derivative X-ray absorption near edge structure (XANES) for pristine $LaFeO_3$, Mg^{2+} substituted La deficient $LaFeO_3$ ($La_{1-x}FeO_{3-\delta}$; xMg, x = 0.2 and 0.4) and Fe deficient $LaFeO_3$ ($LaFe_{1-x}O_{3-\delta}$; xMg, x = 0.2 and 0.4) ceramics.*

It is noticed from the inset that, in La deficient compositions, the pre-edge intensity increases while the white line area decreases with increasing Mg^{2+} content. This suggests the changes in the geometry around Fe ions, transitioning from the centro-symmetric arrangements in pristine $LaFeO_3$ and introduction of crystal structural distortion.[25] The geometric changes and structural distortion are more pronounced in La deficient samples than in Fe deficient ones. Additionally, the edge jump for La-deficient Mg^{2+}-incorporated samples shifts towards lower energy compared to pristine $LaFeO_3$ and Fe-deficient Mg^{2+}-incorporated compositions. First derivative analysis of the Fe K-edge XANES confirms that the main absorption edge remains at ~7124 eV in all samples, indicating that Fe predominantly exists in the 3+ oxidation state (Fe^{3+}) oxidation.

To investigate the local structural environment around Fe ions, Fe K-edge EXAFS spectra were analyzed in both k-space and their corresponding Fourier transforms in R-space (Figs. 11a and 11b). Significant changes in the path amplitude of the EXAFS oscillation are observed in both La- and Fe-deficient Mg^{2+}-incorporated $LaFeO_3$ samples compared to pristine $LaFeO_3$, indicating alterations in the local Fe environment. Fourier transforms of the Fe K-edge EXAFS spectra for pristine $LaFeO_3$ show three distinct peaks at radial distances ~1.5, 3.0, and 3.5 Å corresponding to the Fe-O, Fe-La, and Fe-Fe scattering paths, respectively, along with smaller peaks at 2.1 and 2.5 Å attributed to spectral leakage.[26] The Fe–O peak position remains largely unchanged across all compositions, suggesting that the average Fe–O bond length is preserved. However, Fe–O peak amplitude decreases in both La- and Fe-deficient samples upon Mg^{2+} incorporation, indicating a reduction in Fe–O coordination number, likely due to local structural distortions. In contrast, Fe–La and Fe–Fe peaks show amplitude variations and slight positional shifts upon Mg^{2+} incorporation, supporting the presence of structural rearrangements. In La-deficient compositions, a new prominent peak at ~2.6 Å emerges, assigned to Fe–Mg interactions, while the Fe–La peak at ~3.0 Å decreases in intensity - consistent with Mg^{2+} occupying La^{3+} sites (Fig. 11c). The Fe–Mg peak intensity increases with higher Mg content, while the Fe–Fe peak position remains unchanged. In the Fe-deficient samples, the relative intensities of the Fe–Mg and Fe–La peaks (~2.6 Å and ~3.0 Å), remain nearly unchanged (Figure 11d), but the Fe–Fe peak shifts to a higher radial distance, indicating alterations in Fe–Fe spacing due to Mg^{2+} substituting at Fe^{3+} sites. These results collectively suggest that Mg^{2+} acts as an amphoteric substituent, occupying both A-site (La^{3+}) and B-site (Fe^{3+}) positions in the perovskite lattice, thereby inducing substantial local structural distortions in both La- and Fe-deficient $LaFeO_3$ ceramics.

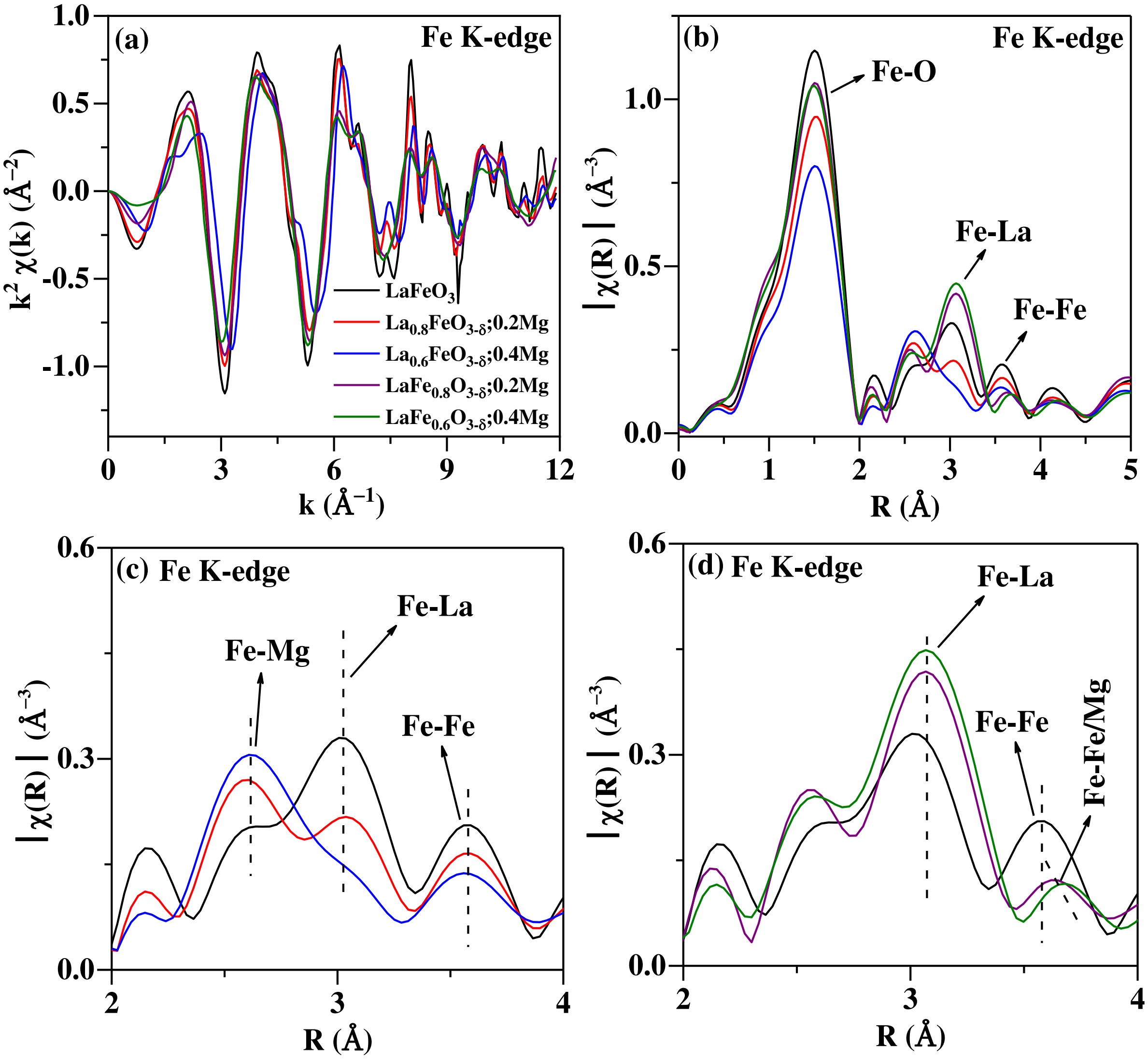

Fig. 11: *Fe K-edge (a) EXAFS signals in k-space and (b) Fourier transform of EXAFS signals in R-space for pristine* $LaFeO_3$*,* Mg^{2+} *substituted La deficient* $LaFeO_3$ *(*$La_{1-x}FeO_{3-\delta}$*; xMg, x = 0.2*

and 0.4) and Fe deficient LaFeO$_3$ *(LaFe*$_{1-x}$*O*$_{3-\delta}$*; xMg, x = 0.2 and 0.4) ceramics. (c, d) Magnified image of (b) in the region of radial distance 2 to 4 Å for pristine LaFeO*$_3$ *with Mg*$^{2+}$ *substituted (c) La deficient LaFeO*$_3$ *and (d) Fe deficient LaFeO*$_3$ *ceramics.*

To investigate the local structural environment around Fe ions, further analysis of the Fe K edge EXAFS spectra were performed to extract the Fe-O coordination number and nearest neighbor distances. The experimental EXAFS spectra, represented as $k^2\chi(k)$, and corresponding Fourier transforms, along with the fitted curves, are shown in Figs. 12a and 12b. Fitting was carried out in the k range of 3-10 Å^{-1} and the R range of 1-4 Å. The fitted structural parameters - coordination number (N), bond-distance (R), Debye-Waller factor (σ^2), and inner-potential shift (ΔE_0) - are listed in Table 5. In pristine LaFeO$_3$, Fe atoms exhibit octahedral coordination, with Fe-O coordination number of 5.7±0.3 and an average bond length of 1.994±0.002 Å. Fe-La and Fe-Fe bond distances are 3.304±0.007 Å and 3.960±0.013 Å, respectively. In La-deficient Mg^{2+} - incorporated samples (La$_{1-x}$Mg$_x$FeO$_{3-\delta}$:x = 0.2 and 0.4), the Fe-O coordination number decreases to 5.2±0.1 and 5.0±0.1, with corresponding bond lengths of 1.997±0.002 Å and 1.998±0.002 Å. The reduction indicates V$_O$ formation. Notably, a prominent Fe-Mg scattering path emerges in these samples, with coordination number of 1.6±0.4 and 3.1±0.9, and bond lengths of 2.963±0.019 Å and 2.910±0.012 Å for x = 0.2 and 0.4, respectively. These path lengths are shorter than the Fe–La distances, likely due to the higher electron affinity of Mg^{2+} compared to La^{3+}. Increasing Mg^{2+} content raises the Fe–Mg coordination numbers while reducing bond lengths, indicating enhanced local distortion. A slight elongation of the Fe–La bonds to 3.326 ± 0.012 Å and 3.277 ± 0.020 Å is also observed, compared to the pristine composition, which can be attributed to Mg^{2+} substitution at La^{3+} sites. Meanwhile, the Fe–Fe bond distances remain largely unchanged, suggesting minimal substitution of Mg^{2+} at Fe^{3+} sites. In Fe deficient

Mg^{2+}-incorporated samples ($LaFe_{1-x}Mg_xO_{3-\delta}$; $x = 0.2$ and 0.4), Fe–O coordination numbers are 5.4 ± 0.2 and 5.3 ± 0.2, again indicating the presence of V_O. These samples also show slightly reduced Fe–O bond lengths, along with increased Fe–La and Fe–Fe/Mg scattering path lengths, confirming local structural distortion induced by Mg^{2+} substitution at Fe^{3+} sites.

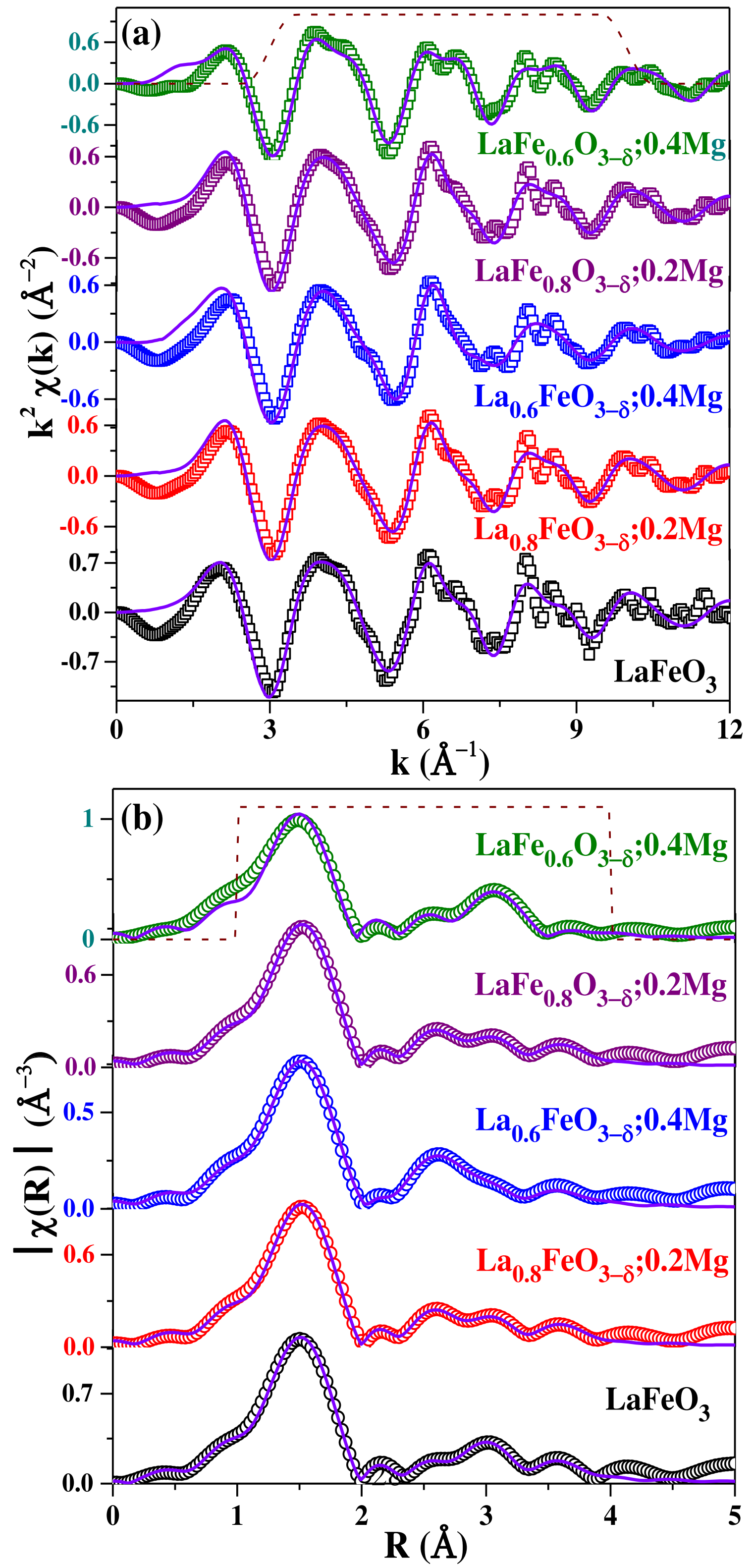

Fig 12: *Fe K-edge (a) EXAFS signals and (b) Fourier transform of EXAFS signals for pristine* $LaFeO_3$, Mg^{2+} *substituted La deficient* $LaFeO_3$ ($La_{1-x}FeO_{3-\delta}$; *xMg, x* = 0.2 *and* 0.4) *and Fe deficient* $LaFeO_3$ ($LaFe_{1-x}O_{3-\delta}$; *xMg, x* = 0.2 *and* 0.4) *ceramics. Open symbols, solid lines, and the window represent the experimental data, fitted curve, and the fitting range respectively.*

Table 5: *Simulated parameters from Fe K-edge EXAFS signals of pristine* $LaFeO_3$, Mg^{2+} *substituted La deficient* $LaFeO_3$ ($La_{1-x}FeO_{3-\delta}$; *xMg, x* = 0.2 *and* 0.4) *and Fe deficient* $LaFeO_3$ ($LaFe_{1-x}O_{3-\delta}$; *xMg, x* = 0.2 *and* 0.4) *ceramics. The parameters are coordination number (N), bond distance (R), inner potential shift* (ΔE_0)*, and Debye-Waller factor* (σ^2)*. The goodness of fit is represented by the R-factor.*

Samples	Shells	Parameters				R-factor
		N	R (Å)	ΔE_0 (eV)	σ^2 (Å^2)	
$LaFeO_3$	Fe-O	5.7±0.3	1.994±0.002	1	0.003	0.004
	Fe-La	8	3.304±0.007	−10	0.017	
	Fe-Fe	6	3.960±0.013	−15	0.017	
$La_{0.8}FeO_{3-\delta}$; 0.2Mg	Fe-O	5.2±0.1	1.997±0.002	2.7	0.003	0.007
	Fe-Mg	1.6±0.4	2.963±0.019	3.4	0.010	
	Fe-La	5.7±0.8	3.326±0.012	−8.2	0.019	
	Fe-Fe	6	3.959±0.012	−15	0.016	
$La_{0.6}FeO_{3-\delta}$; 0.4Mg	Fe-O	5.0±0.1	1.998±0.002	3	0.005	0.003
	Fe-Mg	3.1±0.9	2.910±0.012	−3.6	0.012	
	Fe-La	4.5±0.7	3.277±0.020	−4.5	0.023	
	Fe-Fe	6	3.956±0.020	−14	0.023	
$LaFe_{0.8}O_{3-\delta}$; 0.2Mg	Fe-O	5.4±0.2	1.982±0.003	2	0.002	0.017
	Fe-La	8	3.355±0.010	−5.6	0.014	
	Fe-Fe/Mg	6	4.044±0.036	−10	0.023	
$LaFe_{0.6}O_{3-\delta}$; 0.4Mg	Fe-O	5.3±0.2	1.975±0.004	1	0.002	0.022
	Fe-La	8	3.367±0.012	−5	0.014	
	Fe-Fe/Mg	6	4.032±0.032	−11	0.030	

IV. Summary and Conclusions

In this work, the structural, optical, electrical and magnetic properties of pristine $LaFeO_3$ and effect of Mg^{2+}-incorporation in $LaFeO_3$ ceramics have been investigated, focusing on two different cases: (i) La-deficient $LaFeO_3$ ($La_{1-x}FeO_{3-\delta}$; xMg, $x = 0.2$ and 0.4) and (ii) Fe-deficient $LaFeO_3$ ($LaFe_{1-x}Mg_xO_{3-\delta}$; $x = 0.2$ and 0.4). Structural analysis confirms that in La-deficient $LaFeO_3$, Mg^{2+} ions partially substitute La^{3+} sites, leading to the formation of oxygen-vacancy defects (V_O) and secondary phases such as γ-Fe_2O_3 and $MgFe_2O_4$ appear at $x = 0.4$. Similarly, in Fe-deficient $LaFeO_3$, partial substitution of Fe^{3+} sites by Mg^{2+} results in V_O defects and the formation of secondary phase La_2O_3 is noted at $x = 0.4$. The structure-property correlations between these two different Mg^{2+}-incorporated $LaFeO_3$ ceramics are compared with those of pristine $LaFeO_3$ ceramics.

(i) Mg^{2+}-incorporated La-deficient $LaFeO_3$ ceramics exhibit a reduced in bandgap (2.23 and 2.30 eV) compared to pristine $LaFeO_3$ (2.34 eV), while Fe-deficient $LaFeO_3$ ceramics do not display a well-defined bandgap. The bandgap reduction and diffused bandgap are attributed to oxygen-vacancy-induced mid-bandgap defect states.

(ii) Mg^{2+}-incorporated La-deficient $LaFeO_3$ ceramics show a pronounced enhancement in magnetization compared to pristine $LaFeO_3$, whereas Fe-deficient $LaFeO_3$ ceramics exhibit weak ferromagnetism. The strong magnetization in the La-deficient case arises from modification in the hybridization between Fe(3*d*)-O(2*p*), La(5*d*)-O(2*p*) and Fe(4*sp*)-O(2*p*) states, along with contributions from uncompensated surface spins and canted internal spins caused by the changes in electronic structure.

(iii) Mg^{2+}-incorporated La-deficient $LaFeO_3$ ceramics show a larger bifurcation between ZFC and FC magnetization curves compared to pristine $LaFeO_3$, whereas Fe-deficient $LaFeO_3$ ceramics display an additional magnetic transition at 88 K in ZFC curve. This transition correlates with electronic structure changes, as evidenced by the appearance of a pre-peak at O K-edge.

(iv) XANES, an element specific characterization confirms the oxidation states of La^{3+} and Fe^{3+} in pristine, La deficient, and Fe deficient $LaFeO_3$ ceramics without showing any significant changes in oxidation states. The substitution of Mg^{2+} at La^{3+} sites in La deficient $LaFeO_3$ ceramics and at Fe^{3+} sites in Fe deficient $LaFeO_3$ ceramics are confirmed by EXAFS studies.

Supplemental Material

See the supplementary material for the figures of X-ray diffraction pattern corresponding to the (121) plane, changes in the lattice parameters and volume, William-Hall plot, EDS spectra, NEXAFS spectra of La $M_{4,5}$-edge of pristine $LaFeO_3$, Mg^{2+} incorporated La deficient $LaFeO_3$ ($La_{1-x}FeO_{3-\delta}$; xMg, $x = 0.2, 0.4$) and Fe deficient $LaFeO_3$ ($LaFe_{1-x}O_{3-\delta}$; xMg, $x = 0.2, 0.4$) sintered ceramics.

ACKNOWLEDGMENTS

We acknowledge DESY (Hamburg, Germany), a member of the Helmholtz Association HGF, for the provision of experimental facilities. Part of this research was carried out at PETRA III, P64 and we would like to thank Dr. Aleksandr Kalinko for beamline guidance.

References

1. A. Scholl, J. Stöhr, J. Lüning, J. W. Seo, J. Fompeyrine, H. Siegwart, J.-P. Locquet, F. Nolting, S. Anders, E. E. Fullerton, M. R. Scheinfein and H. A. Padmore, Science **287** (5455), 1014-1016 (2000).
2. J. Qin, Z. Cui, X. Yang, S. Zhu, Z. Li and Y. Liang, Sensors and Actuators B: Chemical **209**, 706-713 (2015).
3. H. Yamada, Y. Ogawa, Y. Ishii, H. Sato, M. Kawasaki, H. Akoh and Y. Tokura, Science **305** (5684), 646-648 (2004).
4. F. H. Taylor, J. Buckeridge and C. R. A. Catlow, Chemistry of Materials **28** (22), 8210-8220 (2016).
5. S. Revathi, R. Srimathi, A. Kumar, J. Kaur, S. Yuvaraj, M. Ubaidullah, M. Sundararajan, C. Prakash, A. Kumar, S. F. Shaikh, C. Sekhar Dash, M. Sukumar, S. K. Jesudoss and S. Ayyaru, Inorganic Chemistry Communications **168**, 112777 (2024).
6. T. A. Nguyen, V. N. T. Pham, H. T. Le, D. H. Chau, V. O. Mittova, L. T. Tr Nguyen, D. A. Dinh, T. V. Nhan Hao and I. Y. Mittova, Ceramics International **45** (17, Part A), 21768-21772 (2019).
7. D. Triyono, U. Hanifah and H. Laysandra, Results in Physics **16**, 102995 (2020).
8. Q. Lin, X. Yang, J. Lin, Z. Guo and Y. He, International Journal of Hydrogen Energy **43** (28), 12720-12729 (2018).
9. U. Hanifah and D. Triyono, AIP Conference Proceedings **2242** (1) (2020).
10. Q. Liu, Z. You, S. J. Zeng and H. Guo, Journal of Sol-Gel Science and Technology **80** (3), 860-866 (2016).
11. S. Nandy, M. Theingi, S. Ghosh, K. H. Chae and C. Sudakar, Journal of Applied Physics **136** (10), 103901 (2024).
12. W. A. Caliebe, V. Murzin, A. Kalinko and M. Görlitz, AIP Conference Proceedings **2054** (1) (2019).
13. B. Ravel and M. Newville, Journal of Synchrotron Radiation **12** (4), 537-541 (2005).
14. X. Zhang, Y. Niu, X. Meng, Y. Li and J. Zhao, CrystEngComm **15** (40), 8166-8172 (2013).
15. H. Kabir, S. H. Nandyala, M. M. Rahman, M. A. Kabir and A. Stamboulis, Applied Physics A **124** (12), 820 (2018).
16. A. Cyza, Ł. Cieniek, T. Moskalewicz, W. Maziarz, J. Kusiński, K. Kowalski and A. Kopia, Catalysts **10** (9), 954 (2020).
17. G. Pecchi, M. Jiliberto, A. Buljan and E. Delgado, Solid State Ionics **187** (1), 27-32 (2011).
18. A. Paul Blessington Selvadurai, V. Pazhanivelu, C. Jagadeeshwaran, R. Murugaraj, I. Panneer Muthuselvam and F. C. Chou, Journal of Alloys and Compounds **646**, 924-931 (2015).
19. F. Naaz, H. K. Dubey, C. Kumari and P. Lahiri, SN Applied Sciences **2** (5), 808 (2020).
20. Q. Lin, J. Lin, X. Yang, Y. He, L. Wang and J. Dong, Ceramics International **45** (3), 3333-3340 (2019).
21. Y. Janbutrach, S. Hunpratub and E. Swatsitang, Nanoscale Research Letters **9** (1), 498 (2014).
22. F. Huang, Z. Wang, X. Lu, J. Zhang, K. Min, W. Lin, R. Ti, T. Xu, J. He, C. Yue and J. Zhu, Scientific Reports **3** (1), 2907 (2013).

23. Z. C. Xu, M. F. Liu, C. C. Chen and X. N. Ying, Journal of Applied Physics **115** (12) (2014).
24. M. Abbate, F. M. F. de Groot, J. C. Fuggle, A. Fujimori, O. Strebel, F. Lopez, M. Domke, G. Kaindl, G. A. Sawatzky, M. Takano, Y. Takeda, H. Eisaki and S. Uchida, Physical Review B **46** (8), 4511-4519 (1992).
25. N. G. Imam, G. Aquilanti, S. F. Mansour, Z. K. Heiba and C. Meneghini, Materials Research Express **6** (11), 115502 (2019).
26. S. K. Pandey, S. Khalid, N. P. Lalla and A. V. Pimpale, Journal of Physics: Condensed Matter **18** (47), 10617 (2006).